Accessing the band alignment in high efficiency Cu(In,Ga)(Se,S)$_2$ (CIGSSe) solar cells with an In$_x$S$_y$:Na buffer based on temperature dependent measurements and simulations

Johannes Schoneberg,[1] Jörg Ohland,[1] Patrick Eraerds,[2] Thomas Dalibor,[2] Jürgen Parisi,[1] and Michael Richter[1]

[1]*Laboratory for Chalcogenide Photovoltaics, Department of Energy and Semiconductor Research, Institute of Physics, University of Oldenburg, D-26111 Oldenburg, Germany*
[2]*AVANCIS GmbH, Otto-Hahn-Ring 6, 81739 Munich, Germany*

We present a one-dimensional simulation model for high efficiency Cu(In,Ga)(Se,S)$_2$ solar cells with a novel band alignment at the hetero-junction. The simulation study is based on new findings about the doping concentration of the In$_x$S$_y$:Na buffer and i-ZnO layers as well as comprehensive solar cell characterization by means of capacitance, current voltage, and external quantum efficiency measurements. The simulation results show good agreement with the experimental data over a broad temperature range, suggesting the simulation model with an interface-near region (INR) of approximately 100 nm around the buffer/absorber interface that is of great importance for the solar cell performance. The INR exhibits an inhomogeneous doping and defect density profile as well as interface traps at the i-layer/buffer and buffer/absorber interfaces. These crucial parameters could be accessed via their opposing behavior on the simulative reconstruction of different measurement characteristics. In this work, we emphasize the necessity to reconstruct the results of a set of experimental methods by means of simulation to find the most appropriate model for the solar cell. Lowly doped buffer and intrinsic window layers in combination with a high space charge at the front of the absorber lead to a novel band alignment in the simulated band structure of the solar cell. The presented insights may guide the strategy of further solar cell optimization including (alkali-) post deposition treatments. *Published by AIP Publishing.* https://doi.org/10.1063/1.5017087

I. INTRODUCTION

Cu(In,Ga)(Se,S)$_2$ (CIGSSe) related materials play a major role in thin film photovoltaics, because record efficiencies of 19.2% (Ref. 1) on module scale (30 cm × 30 cm) make them highly relevant for the industry production. The optimization of the CIGSSe technology within the last few decades led to an increase in complexity of the solar cell device, e.g., by the introduction of chemical inhomogeneity[2] or post deposition treatment (PDT).[3] Due to the multitude of possible improvement routes, simulation approaches are attractive to make proposals for further solar cell optimization. During the last two decades, numerous simulation studies were published, with differences in the used simulation platform, the reconstructed measurement characteristics, or the underlying solar cell materials.[4–21] Within these simulation studies, there are only a few which cover the reconstruction of several characterization methods over a broad temperature range with only one simulation model.[4,10] A meaningful model requires the experimental access of as many material properties as possible. These can be provided by the characterization of the completed solar cell device and additionally by the investigation of single layers.

The electro-optical characteristics of the In$_x$S$_y$:Na buffer layer and intrinsic ZnO layer (i-layer) on glass were obtained to access the isolated layer properties. The studies in this work were carried out on solar cells provided by AVANCIS GmbH. The chemical composition of the absorber was investigated by glow discharge optical emission spectroscopy (GDOES). The

solar cells were characterized with respect to external quantum efficiency measurement (EQE), temperature dependent current voltage characterization (IVT), capacitance voltage measurements (CVT), and thermal admittance spectroscopy (TAS). In this work, a simulation model is presented which covers the reconstruction of the aforementioned measurement methods over a wide temperature range. The simulation model stands out with a novel band alignment at the hetero-contact which is based on new findings on the In$_x$S$_y$:Na buffer layer and the intrinsic ZnO layer.

The organization of the paper is as follows: A general discussion of the experimental findings in Sec. III is the basis for the simulation model which is introduced in Sec. IV. The parameters are adjusted according to the successful simulative reconstruction of the experimental findings. In Sec. IV A, the focus is on the absorber bulk, whereas crucial parameters of the region near the front interface of the absorber are discussed in Sec. IV B. The validation of the simulation model with respect to the derived parameter set and model features is conducted in Sec. V.

II. EXPERIMENTAL METHODS

The investigated CIGSSe solar cells were processed by AVANCIS GmbH and exhibit the layer sequence back electrode/Mo(Se,S)/Cu(In,Ga)(Se,S)$_2$/In$_x$S$_y$:Na/i-ZnO/n-ZnO.[22] The absorber layer was produced by rapid thermal processing of stacked elemental layers in sulfur atmosphere (RTP-SEL).[23] The Mo(Se,S)$_2$ layer forms reactively during the

RTP-step. The front electrode as well as the buffer and i-layer was deposited by sputtering and thermal evaporation. Single layers of In_xS_y:Na and i-ZnO on witness glasses were prepared within the deposition process of the investigated solar cell layer stack. The cell material was produced on modules with the size of $30\,cm \times 30\,cm$ in a research and development pilot line. The solar module consists of monolithically interconnected cells. For the presented investigation, eight small solar cells with an active area of approximately $0.4\,cm^2$ were cut from the module. The cells were contacted without a grid via the neighboring cells front or back contact, respectively.

To ensure the homogeneity within the samples, all solar cells were characterized by means of current voltage, EQE, capacitance voltage, and capacitance frequency measurements at room temperature. Afterwards, two representative samples were investigated by means of IVT, CVT, and TAS, while GDOES measurements were conducted on two neighboring samples.

The IVT measurements in the dark and at a light intensity of $1000\,W/m^2$ were performed in a Cryovac closed-cycle helium contact gas cryostat in a temperature range of 100 K to 300 K. These measurements were conducted with a Keithley 2400 sourcemeter in a four-wire configuration. For TAS and CVT profiling, a Lake Shore closed-cycle helium cryostat was used in a temperature range of 40 K to 330 K. These measurements were performed using a Solartron impedance analyzer SI-1260 in a four-wire configuration. EQE was measured with a Bentham PVE300 system, equipped with an integrated Ulbrichts sphere for reflection measurements. GDOES measurements were carried out with a Spektruma Analytik GDA 750 analyzer.

For the conductivity measurements of the single layers, the transfer length method was applied.[24] The details of the sample preparation for this method are provided in Ref. 25. The conductivity was measured with a Keithley 617 electrometer sourcemeter. The optical characterization of the single layers was performed with a Woolham VASE rotating analyzer ellipsometer in the wavelength range of 300 nm to 1300 nm.

The simulation software employed for this work was Sentaurus TCAD from Synopsys.[26]

III. EXPERIMENTAL RESULTS

A. Electro-optical characterization of buffer and i-layers

The electrical characterization of single layers gives access to the conductivity σ which is the product of the doping density N_d, the mobility of the majority charge carriers μ_n, and the charge of the particle q, according to Eq. (1) (Ref. 24)

$$\sigma = q \cdot N_d \cdot \mu_n. \tag{1}$$

A detailed presentation of the conductivity investigation of In_xS_y:Na is provided in Ref. 25. For i-ZnO, the same procedure was applied. The electrical characterization results in a low conductivity of $1 \times 10^{-5}\,\Omega cm^{-1}$ in the case of the In_xS_y:Na buffer layer and $1 \times 10^{-2}\,\Omega^{-1}cm^{-1}$ for the i-ZnO

layer, which is relatively low compared to values which are assumed in former simulational work.[27] Presuming a typical charge carrier mobility of $(10\text{--}100)\,cm^2/Vs$ for polycrystalline materials,[28] it is possible to suppose a range for the doping density of $(1 \times 10^{12}\text{--}1 \times 10^{13})\,cm^{-3}$ for the In_xS_y:Na layer and $(1 \times 10^{15}\text{--}1 \times 10^{16})\,cm^{-3}$ for the i-ZnO layer. The simulation of the solar cell behavior showed that for lower doping densities the solar cell characteristics are not sensitive to changes within one order of magnitude of this parameter.

A meaningful simulation of the optical behavior of the layer stack depends on the knowledge of the characteristics of the single layers, which are practically accessed by witness glasses. The absorption behavior of both layers is of high importance for the interpretation of the EQE measurements since it gives insight into the origin of current contribution to the EQE at different wavelengths. The required optical properties of the buffer and the i-ZnO layer were determined via spectroscopic ellipsometry measurements analogous to Refs. 6 and 25. Even though the transferability of the results of the single layer characterization to material properties within a solar cell device might be questionable, this approach offers an estimation of solar cell parameters which are otherwise not directly accessible.

B. Capacitance measurements

The TAS and CVT measurements present a very powerful method for the investigation of the defect level and doping distribution in the solar cell. The static charge of ionized doping and defect levels gives a capacitance contribution which has a frequency and temperature dependence due to the energetic and spatial distribution of the defect and doping levels.[29] The TAS results (Fig. 1) show three step signatures N0-N2 whose origins are discussed in the literature.

The step N0 at high frequencies is commonly assigned to the doping of the absorber since it can be linked to a very low activation energy.[30] The signature N1 shows the strongest manifestation in the recorded curves. The physical origin of the N1 step is a matter of debate in the literature,[4,10,30–32] including defect levels or band barriers at different locations. Recent studies which combined simulation and experimental work on solar cells similar to this work attribute the origin of
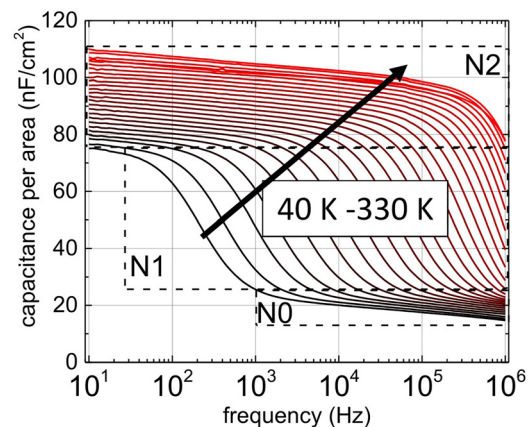

FIG. 1. TAS spectra at zero voltage bias. The capacitance is normalized to the solar cell area. The signatures N0-N2 are discussed in the text.

the N1 signature to a valence band barrier (VBB) located at the back of the absorber.[4,10] The signature N2 can be seen for high temperatures and low frequencies, which is why it is assigned to defects with a high energetic distance to the corresponding band.[4,30,33]

Applying different DC voltages during capacitance measurements leads to a change in the width of the space charge region (SCR) which enables access to the spatial doping and defect distribution.[29] The CVT curves in Fig. 2 show a strong increase in capacitance for positive voltages, which can be attributed to a region with increased doping density near the hetero-junction.

In the literature, this layer is referred to as p^+-layer.[34] Moreover, the increase in the capacitance signal at positive voltages shows a temperature dependent manifestation that we ascribe partly to deep defects.

C. External quantum efficiency

The EQE measurements (Fig. 3) contain information about the generation of electron-hole pairs and their subsequent separation and collection.

If the absorption behavior of the layer stack is known, the EQE can be used to access the electrical parameters, which are of high relevance for the solar cell. The EQE in the long wavelength range between 800 nm and 1100 nm is at a high level compared to samples from the literature,[4,21] due to a low free charge carrier absorption (FCA) and a grading of the band gap E_g (this is known from absorption measurements) in combination with a sufficient diffusion length of the minority charge carriers.[35] The EQE in the range of 350 nm–500 nm is remarkably high compared to values from the literature[4,21] which can be correlated with charge carrier generation in the buffer layer[25] and the subsequent charge carrier collection. In contrast to the buffer, i-ZnO, with a slightly lower band gap compared to n-doped ZnO,[6] has a poor charge carrier separation probability as the EQE in the range of 300 nm–350 nm suggests.

D. IVT

The IVT measurements are suitable to access detailed device parameters, e.g., defect densities, capture cross sections, or barriers in the band structure, by correlating the temperature
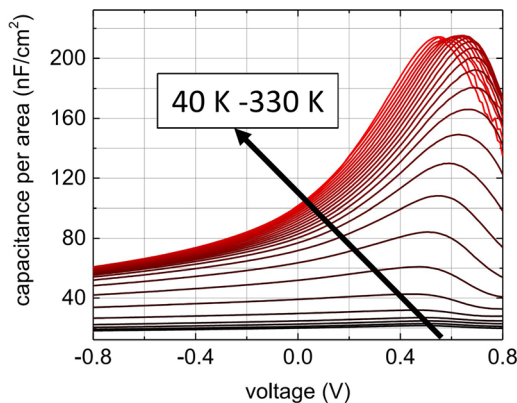

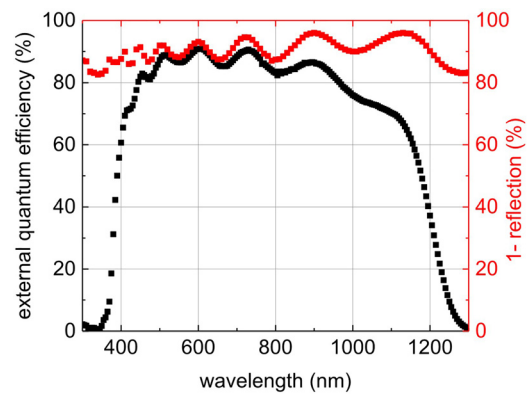FIG. 2. CVT curves for different temperatures measured at a frequency of 10 kHz.

FIG. 3. EQE and 1-reflection versus the wavelength at room temperature.

dependence of the physical models and parameters used in the simulation with the experimental results. The temperature dependence of the open circuit voltage (V_{oc}) and the fill factor (FF) can be seen in Fig. 4. The V_{oc} shows a linear increase with decreasing temperature, which can be related to the temperature dependence of recombination processes.

The extrapolation to low temperatures led to an activation energy of $E_A = 1.1$ eV. The FF increases with decreasing temperature for the same reason down to approximately 200 K, where temperature dependent limitations of the transport led to a drop in the FF. Compared to the literature,[4,21] the transport of charge carriers works very efficiently down to low temperatures of 180 K, which is indicative of a band alignment with small barriers.

IV. MODELING RESULTS

The simulation model contains several features which are motivated by the experimental findings presented in Sec. III. Besides the standard properties which characterize each material in the solar cell, the simulation model exhibits layers with spatial grading of material properties, interface traps, and a doping and defect landscape obtained by the TAS and CVT findings. The set of parameters which is necessary to describe the solar cell stack is shown in Table I. Most parameters can
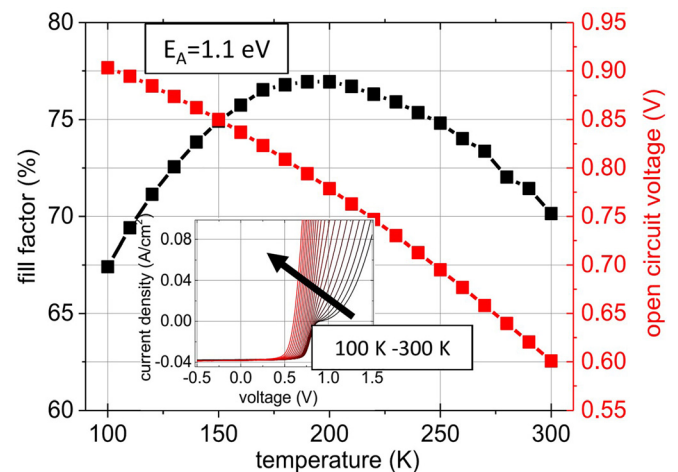

FIG. 4. FF and V_{oc} as a function of the temperature extracted from IVT measurements under illumination (inset). The activation energy is derived by the extrapolation of the V_{oc} to 0 K.

TABLE I. Summary of the set of parameters: band gap E_g, electron affinity χ (work function W_f for metals, respectively), doping density $N_{A/D}$, density of states $N_{V/C}$, electron and hole mobility $\mu_{n/p}$, dielectric constant ε, and electron and hole capture cross sections $\sigma_{n/p}$. The coloring shows groups of parameters which are described in the text.

Positon material	Window n-ZnO	i layer i-ZnO	IF i-ZnO/In$_x$S$_y$:Na	Buffer In$_x$S$_y$:Na	IF In$_x$S$_y$:Na/CIGSSe	Absorber	Back contact Mo(Se,S)$_2$	Mo
E_g[eV]	3.3			2.3		1–1.7	1.36–2.26	…
X[eV]	4.4			4.38		3.95–4.5	4.11	$W_f = 5.2$
$N_{A/D}$[cm^{-3}]	2×10^{20}	1×10^{16}		1×10^{13}		4×10^{16}–5.4×10^{16}	7×10^{15}	…
N_V[cm^{-3}]	1.8×10^{19}			1.8×10^{19}		7×10^{18}	1×10^{19}	…
N_C[cm^{-3}]	4×10^{18}			2.2×10^{18}		2.2×10^{17}	2.2×10^{17}	…
$\mu_{n/p}$[cm^2/V s]	30/30			10/2.5		100/25	100/25	…
N_t[cm^{-3}]	1.7×10^{13}		9×10^{12}	8×10^{13}	3.5×10^{12}	1.6×10^{17}/2.5×10^{14}	3×10^{15}	…
ε	9			10		13	44	
σ_n[cm^2]	1×10^{-13}		1×10^{-13}	4×10^{-13}	2×10^{-13}	1×10^{-16}/2×10^{-14}	1×10^{-15}	
σ_p[cm^2]					2×10^{-14}	5×10^{-13}/5×10^{-11}		…

be taken from literature[4] or can be fitted to device characteristics (black and red numbers in Table I, respectively), whereas others are accessed by measurements of single layers (blue numbers in Table I). The absorber layer is the most complex material since some of its parameters exhibit a spatial grading.

The calibration of the parameters of the absorber will be discussed in the first part of this section. Moreover, the experimental results imply relevant effects taking place in a region in the vicinity of the buffer/absorber interface (interface-near region—INR). This region covers the buffer and i-layer as well as approximately the first 100 nm of the absorber layer, containing two interfaces with traps, as well as defects with a high distance to the corresponding band and an increased doping density in the front part of the absorber. Thus, the parameters of the INR (red numbers in Table I) have a very strong influence on the behavior of the solar cell. The second section focuses on the adjustment of these parameters and their interactions with each other. The simulative reconstruction of the experimental characteristics will be presented afterwards.

A. Adjusting the absorber bulk

1. Grading of the band gap and electron affinity

The gradings of the band gap and the electron affinity were adjusted to the results of GDOES measurements where both values were calculated from the measured chemical composition with the equations according to Ref. 8. The resulting band gap profile (Fig. 5) shows a strong widening towards the backside of the absorber which follows an almost linear behavior and is induced by the indium by gallium and the selenium by sulfur replacement in the crystal structure.

The major part of the shift in the band gap affects the conduction band, which leads to an enhanced minority charge carrier collection from the back of the absorber. Additionally, the band gap profile shows an increase at the front side of the absorber, induced by a selenium by sulfur replacement. This front grading is applied to achieve a reduced recombination at the front of the absorber. The band gap profile and the activation energy E_A derived from IVT analysis suggest the position of dominant recombination to be within the absorber,

i.e., the dominant recombination takes place in the front part or in the back part of the absorber ($E_A > 1$ eV).

2. Doping and defect landscape

Information on the doping and defect landscape can be accessed by the simulative reconstruction of the TAS and the CVT measurements. The N0 signature was assigned to the freeze-out of the doping concentration. However, in the temperature range between 150 K and 300 K which is covered by the simulation this effect is not visible. The activation energy of doping is assumed to have a typical value of 40 meV,[4] The density of the doping was adjusted to the capacitance signal at negative voltages. The signature N1 is interpreted to have its origin from a valence band barrier (VBB) located at the interface between CIGGSSe and Mo(Se,S)$_2$.[4,10] This valence band barrier was realized by a valence band offset (VBO) of $E_{VBO} = E_{V,CIGSSe} - E_{V,MoSSe} = 260$ meV which was obtained by matching the frequency dependence of the signature of the TAS measurements (Fig. 1). For low frequencies and high temperatures, the TAS measurements show a capacitance increase (N2-signature), which is assigned to deep defects. The deep defects are acceptor like since the space charge of the p-type doping level and the defect level have to add up to
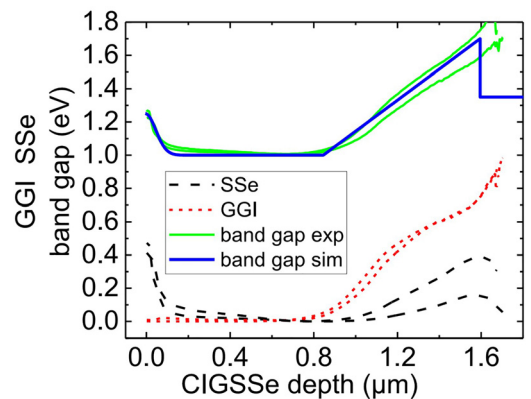

FIG. 5. Calculated gallium to indium (GGI, dotted red line) and sulfur to selenium (SSe, dashed black line) ratio from measured GDOES spectra (not shown). The band gap (green line) is determined by equations from Ref. 8. All steps were conducted on two exemplary solar cells. The blue band gap profile is used as the simulation input.

explain the capacitance signal. Additionally, the CVT curves at positive voltages show a temperature dependent increase (Fig. 2), which suggests an interface near location of the deep defects. Therefore, deep acceptor defects with an energy distance of 850 meV (Ref. 4) to the corresponding valence band, an energetic distribution of 300 meV, and a small spatial distribution close to the absorber/buffer interface are implemented in the simulation model. To account for bulk recombination, mid-gap defects with an energy width of 300 meV (Ref. 4) distributed over the whole depth of the absorber are assumed. In contrast to the literature,[4] these bulk defects cannot be linked to a specific step signature in the TAS. This can be explained by the strong manifestation of the N1 step. However, the existence of recombination centers within the absorber is very likely, even in high quality absorbers and mid-gap defects with a broad energetic distribution are a reasonable approximation. The exact energetic position as well as the energy distribution underlies an uncertainty of approximately 50 meV in which a variation does not significantly vary the simulation output.

The profiles of the doping and defect densities are accessed via CVT measurements. Applying a positive voltage to a solar cell leads to an increase in the capacitance which can be analyzed by the Mott Schottky plot.[36] In the case of homogeneous doping, the Mott Schottky curve follows a linear behavior, whereas a curvature suggests an inhomogeneous doping concentration. The observed temperature dependence of the CVT curves in the range of positive voltages can be correlated with the deep acceptor defects postulated due to the N2-signature, since their energetic distance to the valence band does not allow for a capacitance contribution at lower temperatures or higher frequencies. The evaluation of the width of the SCR under the assumption of a plate capacitor[36] leads to a low SCR width of around 100 nm. If the roughness of the absorber and the width of the SCR are in a similar range, there might occur a mismatch in area rescaling of the projected cell area.[5] Therefore, a larger effective area to rescale the capacitance data is necessary. The absorber roughness was investigated by scanning electron microscopy with the result of an effective area enlargement of approximately 10% compared to the measured cell area. For the further modeling, the capacitance data were rescaled to the calculated effective area.

3. Recombination in the bulk

The minority carrier diffusion length can be investigated by the simulation of the EQE at long wavelengths,[37] since the optical data of every material are measured or are known from the literature.[6] For the derived SCR of approximately 110 nm, the high EQE at long wavelengths suggests a good carrier transport from the bulk and consequently a high minority carrier diffusion length. To match this behavior in the simulation, the bulk recombination rate has to be set on a low value. Since the density of defects and therefore the space charge contribution are already fixed by the CVT measurements, the adjustments of the simulated EQE enable access to the capture cross section of the defects. The uncertainty of the energetic position and distribution of the defects affects the value of the capture cross section. However, the translated uncertainty in the capture cross section is relatively

low within one order of magnitude. The capture cross section is chosen asymmetrically for electrons and holes, which gives the opportunity to control the charge of defect levels positioned between the two quasi-Fermi levels (QFL).[38] The assumption of asymmetric capture cross sections for electrons and holes for CIGSSe is found in the literature with both tendencies ($\sigma_n \lessgtr \sigma_p$).[13,17,18,39]

4. Back contact

The simulation of the IVT characteristics gives important insights into the recombination mechanisms and the charge carrier collection. However, the separation of the effects of both phenomena becomes a challenge. As mentioned above, the N1 signature of the TAS-measurement can be explained by a VBB of $E_{VBO} = 260$ meV at the back of the absorber. However, a barrier of this height affects the current transport in the IVT simulation, which leads to a severely overestimated roll-over. This conflict was solved by the assumption of lateral back contact variations of the absorber/Mo(Se,S)$_2$ VBO in a 2D simulation study.[5] To account for this effect in an 1D simulation model, the VBB is assumed to be different for the simulation of TAS and IVT ($\Delta E_{VBO} = 100$ meV). As the interface related parameters strongly influence the simulation of IVT, e.g., by the effect of type inversion, the exact simulation of the IVT is addressed in Sec. IV B.

The parameters of the absorber bulk are summarized in Table I. Besides a spatial profile in the band gap, the electron affinity, and the doping concentration, the absorber layer exhibits mid-gap defects located all over the absorber and deep defects located at the INR. Moreover, a VBB at the back of the absorber is suggested.

B. Adjusting the interface-near region

The high resistivity of buffer and i-layer materials as investigated in Sec. III requires reconsidering the model configuration of the INR. In comparison to assumptions stated in the literature (also relying on CdS history),[10–13,16,21] the conductivity of the In$_x$S$_y$:Na buffer layer regarded in this study is four to seven orders of magnitude lower[4,13] depending on the used buffer layer material (CdS or In$_x$S$_y$:Na), leading to a severely reduced electron mobility and / or doping density [see Eq. (1)]. It needs to be mentioned that this is the first simulation study in which the conductivity of the buffer layer is determined from measurements of a witness layer from the production line of the solar cell. However, by implementing the determined buffer and i-layer mobility and doping concentration in the simulation model, we find a severe impact on the simulation quality. This can be attributed to a high transport barrier causing a FF decrease of more than 2% even at room temperature and an overestimated charge carrier separation within the buffer and i-layer, as it is indicated by an overestimated EQE in the corresponding absorption range. All mismatches can be linked to an increased energy distance between the conduction band at the buffer/absorber interface and the electron QFL [see Fig. 6(c)], i.e., a reduction in type inversion. The electron QFL presents a reference position for the considerations concerning the INR since it is fixed due to the strongly doped n-ZnO layer.
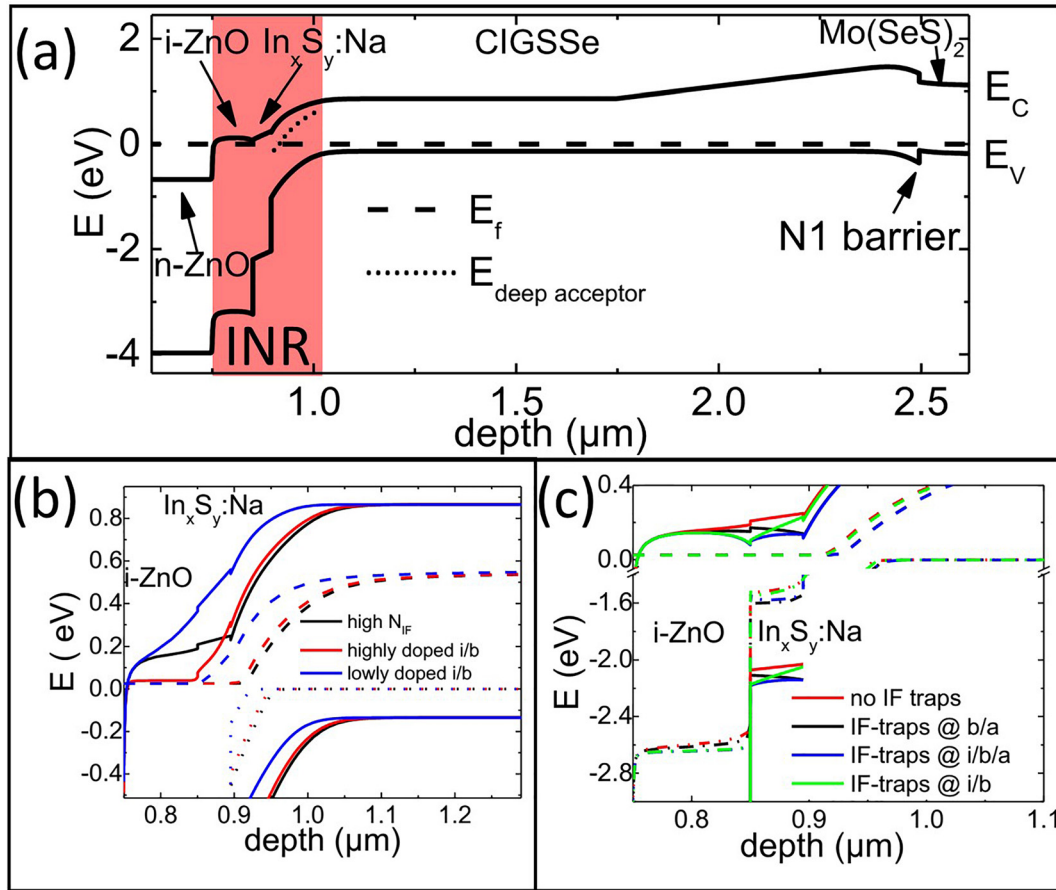
FIG. 6. (a) Simulated band structure of the solar cell (at 0 V and at 300 K in the dark). The hetero-contact band alignment is dominated by lowly doped buffer and i-layer and high interface trap densities. In (b) and (c), the electron QFL (dashed lines), the hole QFL (dotted lines), and the conduction and valence band (solid lines) are shown for different cases. The simulation conditions are 0 V bias, at 300 K and an illumination intensity of 1000 W/m². (b) Influence of the lowly and highly doped buffer and i-layer (i/b). The black line shows the compensating influence of the interface donor traps at the buffer absorber interface. (c) Band structure of the INR for interface traps at the buffer/absorber (B/A), i-layer/buffer (i/b), and both interfaces (i/b/a) configurations. The QFL gradient of the minority carrier type gives indication for a successful charge transport.

Without a compensating effect, the low doping densities of the buffer and i-layer pull the conduction band away from the electron QFL, leading to a reduction of the type inversion (reduced V_{oc}) and to an upward shift of the transport barriers (lower FF). Furthermore, a minority carrier QFL is established within the buffer and i-layer, which supports charge carrier collection in these layers. The most important parameter to match the simulation with measurement results is the increase in the interface donor trap density. This increase has the effect of pulling the conduction band at the buffer/absorber interface towards the electron QFL, restoring type inversion. In sum, the findings of low doping of the buffer and i-layer lead to the necessity to reconsider the properties of the INR with respect to most simulation studies in the literature.

1. Doping and defects

Besides the changes in the parameters of the buffer and i-layer, the space charge contribution derived from the CVT and TAS measurements especially at the INR marks a difference to other simulation studies.[10,31] A sufficient matching of experiment and simulation of the CVT curves is achieved by the subsequent adjustment of the bulk doping density and an increased doping (p^+) and deep defect density at the front

of the absorber (p^+-layer) as described in a previous study[4] (see Sec. V B). With the bulk and p^+-doping, the general shape of the CV-curve is reconstructed, whereas the deep defects account for the temperature dependence especially at high voltages. The spatial shape of doping and defect profiles can be adjusted to the CVT-curves with high precision. Additionally, the capacitance response in the TAS measurement in the range of low frequencies (N2-signature) gives further information about the density of deep defects. If only taking CVT and TAS measurements into account, an excellent fitting quality (not shown) could be realized with very high densities for these three parameters.

2. Accessing the transport barrier

In the band structure, a strong p^+-layer pulls the hole QFL close to the absorber valence band; therefore, the conduction band is pushed upwards in this region. If a positive voltage is applied to the structure, the moderately doped bulk of the absorber is shifted downwards, while the p^+-layer forms a bulge in the conduction band. This bulge is also investigated in other simulation studies[4] and is observed to act as a transport barrier. By only considering the capacitance measurements, the bulge formation strongly dominates

the current transport already at high temperatures. Here it is worth to note that a transport barrier is usually realized by the conduction band offset at the buffer/absorber interface as shown in many studies with a CdS-buffer.[7,14] However, in the present study, the conduction band barrier (CBB) caused by a highly negative space charge in the front part of the absorber already shows a strong impact on the transport properties of the device; therefore, the contribution of the conduction band offset to the barrier is assumed to be small. This assumption is supported by chemical investigations of the band alignment performed previously on a similar system[40] that suggest a low spike ($\Delta E_{CB} = E_{C,InS:Na} - E_{C,CIGSSe} = 100$ meV $\pm$ 100 meV) at the buffer/absorber interface. Even with a very low conduction band offset at the buffer/absorber interface, the high transport barrier induced by the high space charge in the absorber front is in conflict with the simulative reconstruction of the good current transport properties observed in the IVT. The temperature dependence of the FF shown in Fig. 7 reveals a drop in the FF only below 200 K.

The interpretation of the mismatch between simulation and experiment of either capacitive or IVT measurements leads to the following assumptions: i) an increased density of the donor-like interface traps (charge state 0/+), which guarantees a less harmful impact of the conduction band bulge barrier and ii) an asymmetry of the deep defect capture cross sections to account for the different charge states of the defect level depending on the QFL positions.[38] The asymmetry of the deep defect capture cross sections causes a compensational effect on their static charges and can be adjusted to the trade-off between the p$^+$-layer indicated in the capacitive measurements and low transport barrier derived from the IVT measurements. To sum up, a strong interface trap density in combination with a high asymmetry in the capture cross section would be the key feature of the simulation model when taking CVT, TAS, and IVT into account.

3. Defects at the i-layer/buffer interface

In the short wavelength range of the measured EQE, we can see that a successful charge carrier separation in the buffer is present which is not r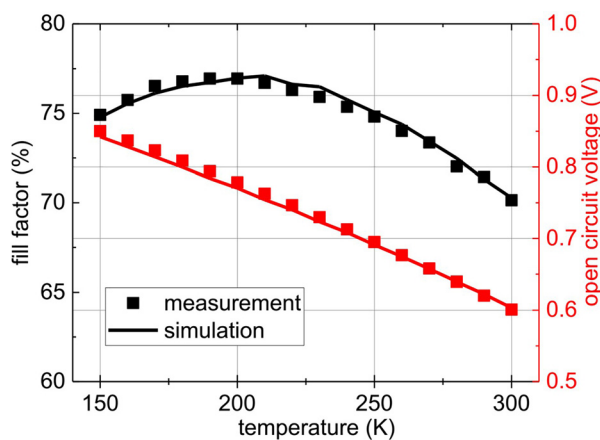econstructed by the simulation at this point. The decisive property is the gradient in the QFL of the minority charge carriers in that region, because the gradient in the QFL represents the electro-chemical force acting on charge carriers. In solar cells with highly doped buffer, the charge carrier separation typically works poorly due to the conduction band being close to the electron QFL [see Fig. 6(b)-black line]. Therefore, the very lowly measured doping density of the buffer layer is in principle accordance with the high EQE. Moreover, the interface trap density can be accessed by matching simulation and experiment of the EQE in that spectral range. Another important observation is the steep decrease in the EQE for wavelengths lower than 350 nm. According to the different absorption behavior of i-ZnO and n-ZnO in that wavelength region, the model predicts a significant charge carrier generation taking place in the i-ZnO.

The low EQE indicates a poor charge carrier collection from this layer. To account for these two observations in the simulation model, donor-like interface traps between the buffer layer and the i-layer are introduced. In general, every hetero-interface is likely to exhibit interface traps; however, in the case of highly doped layers, they might be overlaid by bulk characteristics (see Sec. V B). Consequently, interface traps between the i-layer and buffer layer are implemented in this study, whereas they are neglected at the interface between the front electrode and i-layer. The effect of both interface traps between the i-layer/buffer and buffer/absorber interface on the band alignment can be seen in Fig. 6(c). The conduction band positions at both interfaces are dominated by the interface trap density and can therefore be independently shifted. Consequently, the minority QFL in the buffer and i-layer is affected, thereby determining the charge transport in these layers. Hence, the different EQE contributions from the buffer and i-layer in combination with their low doping densities allow for the independent access to both interface trap densities. It has to be mentioned that the adjustment of the reconstructed EQE by the i-layer/buffer interface traps is a very likely solution, but not the only one. A very low hole mobility in the i-layer ($\mu_p < 1 \times 10^{-6}$ cm^2/Vs) or a strong recombination channel at the interface between the i-layer and front electrode would have a comparable effect on the simulated EQE.

The final model leads to the simulative reconstruction of the characterization results as shown as solid lines in Figs. 7–11. The EQE (Fig. 11) and IVT simulation (Fig. 10) show a good agreement with the experimental data visualized with symbols. The simulated TAS curves (Fig. 8) show general accordance and reconstruct the main step N1. The underestimation of the N2-signature was accepted to guarantee a sufficient current transport. The CVT experiment and simulation (see Fig. 9) show good agreement at negative voltages. The deviations at positive voltages are accepted for a good simulative matching of IVT and EQE. The resulting band diagram at 0 V in the dark is shown in Fig. 6(a).

V. DISCUSSION

A. Set of parameters

In the following, the sensitivity of the simulation results to crucial parameters from Table I are discussed.

FIG. 7. Temperature dependence of measured (symbols) and simulated (lines) fill factor (black) and V$_{oc}$ (red) in the simulated temperature range of 150 K–300 K.
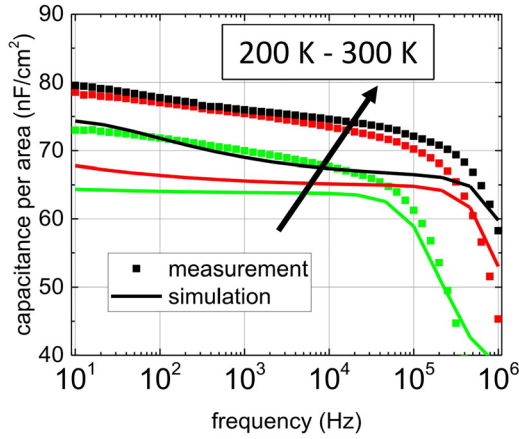
FIG. 8. Measured (symbols) and simulated (lines) C(f) curves for four exemplary temperatures. For temperatures lower than 200 K, the Nyquist plot (not shown) indicates a violation of the equivalent circuit. The measured data are corrected for the effective area approximation.

FIG. 10. Measured (symbols) and simulated (lines) I(V) curves for four exemplary temperatures under illumination and in the dark (inset).

The set of parameters can be divided into three groups where the first one contains layer properties that were accessed via own measurements and deviate from the literature (blue numbers in Table I). A second group comprises parameters that can be either taken from literature references since similar layer properties can be assumed, or can be fitted to device characteristics. These parameters are divided into two subgroups of which one has minor influence on the simulation results (black numbers in Table I) whereas the other group comprises the most crucial parameters for the simulation results (red numbers in Table I). These crucial parameters are the densities of interface traps, deep defects, and p^+-doping, as Sec. IV already indicates.

With the help of Fig. 12, the interplay of these parameters and their effect on the simulative reconstruction of the experimental characteristics of the different applied measurement techniques are illustrated to convey the coherence of the crucial parameters. The traps at the buffer/absorber interface have the strongest effect on the simulative reconstruction of all characterization methods. They dominate the position of the conduction band with respect to the electron QFL position, i.e., a high interface trap density leads to an increased type inversion ($\rightarrow V_{oc}$) and a sufficient current
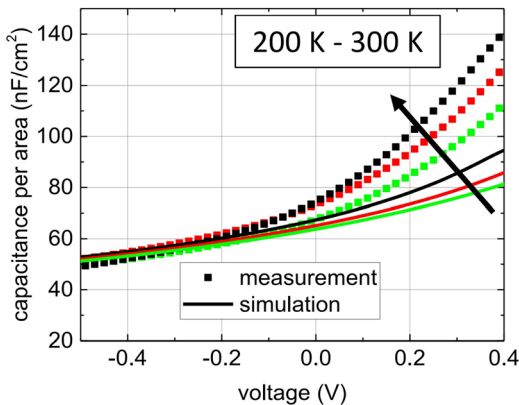
transport ($\rightarrow$FF) on the one hand but reduces the hole QFL gradient of the buffer ($\rightarrow$EQE) on the other hand. The fact that the quality of the simulative reconstruction is counteractive for EQE and IVT when changing the interface trap density enables access of the value in a narrow range of trade-off. Additionally, the position of the conduction band at the buffer/absorber interface influences the electron QFL position in the INR and therefore the charge state of the deep defects which are located in that region. Thus, the density of the interface traps also affects the capacitive simulation ($\rightarrow$CVT/TAS). The same argumentation but with opposite effect holds for the p^+-doping and the deep acceptor defects at the front of the absorber. As a consequence, the change of each of the three parameters increases the reconstruction quality of the results of one characterization method at the cost of causing deterioration in the reconstruction of other characterization results. It has to be mentioned that, even though the discussed trade-off situations enable the access to the respective parameters, an uncertainty of other material characteristics may affect these values. For example, a different energetic position of the mid-gap defects may lead to

FIG. 9. Measured (symbols) and simulated (lines) C(V) curves for four exemplary temperatures. The measured data are corrected for the effective area approximation.
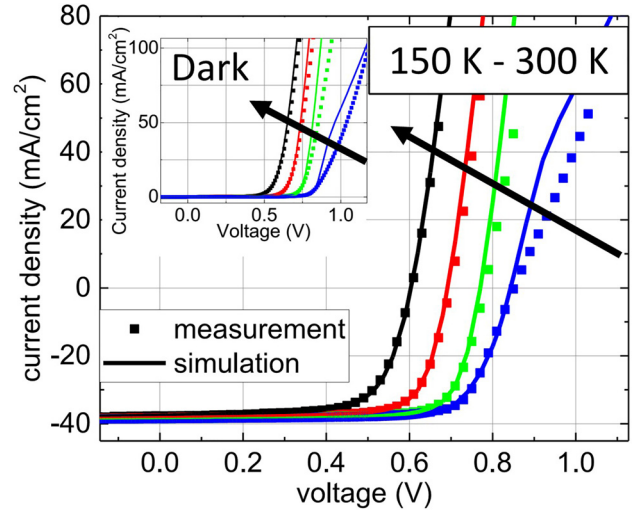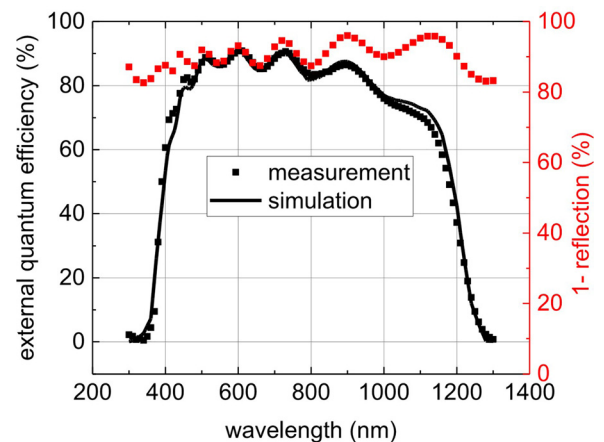

FIG. 11. Measured (symbols) and simulated (lines) EQE curves at room temperatures. The EQE is calculated from the simulated IQE.
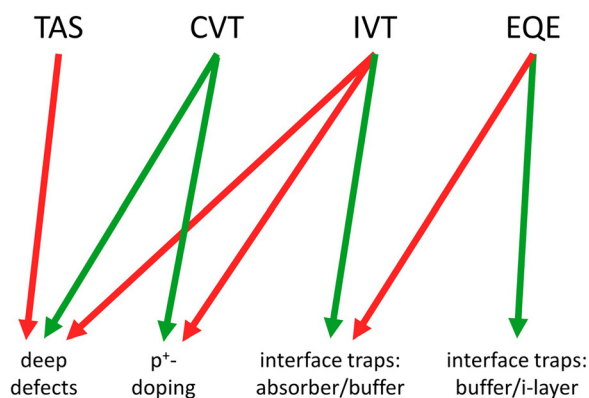
FIG. 12. Visualization of the dominant dependence of the simulative reconstruction quality of the experimental characteristics on crucial parameters in the interface near region. A red arrow depicts an upper limit for the parameters, while a green arrow marks a lower limit. Due to the opposing dependence of modeling quality on the parameter change, the crucial simulation parameters can be accessed in a reliable way.

another trade-off situation and a different set of crucial parameters. Despite the lack of transferability of exact values, the interplay of the crucial parameters and the resulting parameter access remains a meaningful feature of the method of combined simulation and experiments for solar cells with the lowly doped buffer and i-layer.

To summarize, the presented model depends strongly on only a few parameters, which determine the whole performance. But due to the opposing dependence of the reconstruction quality of the different characterization results on the parameters, there is a strong coherence for these parameters with respect to the overall fit quality of the model. The coherence is enhanced by the broad temperature range which is considered by experiment and simulation.

B. Simulation model

The guideline for creating a simulation model should be a sufficient reconstruction of experimental findings with a model of least necessary complexity. In comparison to other simulation studies, the presented model is of increased complexity, but in return it comprises the simulative reconstruction of multiple experimental characteristics at different temperatures. The necessity of specific model features is discussed in the following.

1. Inhomogeneity of the absorber properties

The most complex layer in the investigated solar cells is the absorber, which shows a spatial profile in the band gap, the electron affinity, the optical data, and the doping and defect landscape. The inhomogeneous band structure and consequently the inhomogeneous optical data are well-known features of CIGSSe absorbers and have been the subject of optimization processes.[41] Due to extensive studies on this topic, the corresponding values are either accessible via chemical composition measurements, e.g., GDOES-measurements, or are known from the literature (n,k-data).[42,43] The doping profile as well as the implementation of deep defects is suggested by capacitive measurements and can be correlated with a defect-rich layer near the surface, which is reported by

others[4,34] To our knowledge, an inhomogeneous doping profile is the only suitable approach for explaining the strong capacitance increase at positive voltages.

2. Introduction of interface traps at both sides of the buffer layer

Besides the inhomogeneity of the absorber, a second feature within the presented model is the assumption of interface traps at both sides of the buffer layer. Both interface trap parameters are non-accessible, but in general interface traps are realistic to occur at hetero-contact surfaces.[11] However, since they have a crucial impact on the model behavior, they have to be regarded critically. In the literature, the interface is handled in various ways. While some studies do not account for traps at the interface at all,[15,21,39] others assume an interface recombination velocity while neglecting charge effects[13,18,19] and some assume interface traps.[4,14,16,20] The disregard of static charges at the interface is explicitly critical if the buffer is lowly doped, because in this case the space charges of the interface defects mainly determine the position of the conduction band in the INR. The static charge of a strongly doped buffer layer would overlay the static charge of the interface traps. The latter also gives reason, why in most studies in the literature the strong influence of the interface charges is not seen. The ability to access the interface trap properties is based on the findings of a low conductivity of the buffer and i-layer, materials, which in turn rely on the transferability of single layer properties to the properties in the layer stack. This drawback is inherent for the approach of single layer characterization. In more detail, a doping density of the buffer $N_{buffer} > 1 \times 10^{16} \, cm^{-3}$ would lead to a reduction of the interface trap density and $N_{buffer} > 1 \times 10^{18} \, cm^{-3}$ would inhibit the access to the interface traps. The implementation of traps at the i-layer/buffer interface was gauged to be the most likely scenario among other possible model features like a very low hole mobility in the i-layer or the implementation of interface traps at the n-ZnO/ i-layer interface. The presented simulation model exhibits a small INR with only three parameters determining the whole solar cell performance. This raises the question if such a region gets evidence from the literature. Besides findings of simulation studies,[4] also recent work on post deposition treatment (PDT) gives evidence for the importance of an INR, as the solar cell improvement by PDT is most likely linked to the front part of the absorber.[44]

3. Reasons for the 1D simulation model

Besides the above-mentioned complex features, the consideration of an only one-dimensional model as a simplification has to be discussed. Taking a multi-dimensional modeling for CIGSSe solar cells into account can be of essential importance depending on the goals of the modeling. The explanation of the N1 step by a lateral inhomogeneous valence band barrier and the effective area assumption for capacitance scaling are two approximations which are necessary in the presented model. However, multi-dimensional models also cause a severe increase in the number of parameters of which the lateral variations might not be accessible. Therefore, the calibration to experimental data has to be regarded critically. Besides

this, the modeling time strongly increases with every additional dimension. Hence, if the scope of the investigation is not explicitly focusing on multi-dimensional effects, like voids or monolithic interconnections, e.g., Refs. 5 and 9, a comparably simple and fast one-dimensional simulation model has the advantage of fast calculation times and a smaller set of parameters.

VI. CONCLUSION

In this work, we suggest a novel band alignment for CIGSSe solar cells with an In$_x$S$_y$:Na buffer based on experimental data combined with simulation. The simulation model is based on the temperature dependent device characterization and on new experimental findings on low doping of buffer and i-layer (in our case In$_x$S$_y$:Na as buffer and i-ZnO i-layer). The simulation is capable of modeling the device characteristics of current voltage as well as capacitance measurements in a wide temperature range with a reasonable convergence. The simulation model shows that due to the low doping of buffer and i-layer the interfaces and the absorber region near the buffer/absorber interface have a stronger influence on the solar cell characteristics than for a highly doped buffer and i-layer which is usually assumed in simulation studies. We discussed that the existence of such a region gets evidence from recent work on post deposition treatment (PDT), as the solar cell improvement by PDT is most likely linked to the front part of the absorber.

The combined simulative reconstruction of the above-mentioned experimental characteristics provides unique access to the decisive parameters because of their opposing behavior on the modeled results. The presented simulation is capable of modeling the complex behavior of CIGSSe solar cell over a wide range of temperatures and future work may support the route to further solar cell optimization.

[1]M. Green, Y. Hishikawa, W. Warta, E. Dunlop, D. Levi, J. Hohl-Ebinger, and A. Ho-Baillie, Prog. Photovoltaics Res. Appl. **25**, 668–676 (2017).

[2]R. Knecht, M. Hammer, J. Parisi, and I. Riedel, Phys. Status Solidi A **210**, 1392–1399 (2013).

[3]D. Abou-Ras, S. Wagner, B. Stanbery, H. Schock, R. Scheer, L. Stolt, S. Siebentritt, D. Lincot, C. Eberspacher, K. Kushiya, and A. Tiwari, Thin Solid Films **633**, 2–12 (2017).

[4]M. Richter, I. Riedel, C. Schubbert, P. Eraerds, J. Parisi, T. Dalibor, and J. Palm, Sol. Energy Mater. Sol. Cells **132**, 162–171 (2015).

[5]M. Richter, I. Riedel, C. Schubbert, P. Eraerds, J. Parisi, T. Dalibor, and J. Palm, Phys. Status Solidi A **212**, 298–306 (2015).

[6]M. Richter, C. Schubbert, P. Eraerds, I. Riedel, J. Keller, J. Parisi, T. Dalibor, and A. Avelán-Hampe, Thin Solid Films **535**, 331–335 (2013).

[7]C. Schubbert, P. Eraerds, M. RIchter, J. Parisi, I. Riedel, T. Dalibor, and J. Palm, Phys. Status Solidi A **212**, 336–347 (2015).

[8]C. Schubbert, P. Eraerds, M. Richter, J. Parisi, I. Riedel, T. Dalibor, and A. Avellán, in Proceedings of the 27th EUPVSEC, Frankfurt, Germany (2012).

[9]C. Schubbert, P. Eraerds, M. Richter, J. Parisi, I. Riedel, T. Dalibor, and J. Palm, Sol. Energy Mater. **157**, 146–153 (2016).

[10]T. Eisenbarth, R. Caballero, M. Nichtewitz, C. Kaufmann, H. Schock, and T. Unold, J. Appl. Phys. **110**, 094506–094511 (2011).

[11]M. Burgelman, P. Nollet, and S. Degrave, Thin Solid Films **361–362**, 527–532 (2000).

[12]M. Burgelman, J. Verschraegen, S. Degrave, and P. Nollet, Prog. Photovoltaics: Res. Appl. **12**, 143–153 (2004).

[13]M. Gloeckler, A. Fahrenbruch, and J. Sites, in *3rd World Conference on Photovoltaic Energy Conversion* (2003), pp. 491–494.

[14]G. Sozzi, F. Trone, and R. Menozzi, Sol. Energy Mater. Sol. Cells **121**, 126–136 (2014).

[15]G. Sozzi, M. Lazzarini, R. Menozzi, R. Carron, E. Avancini, B. Bissig, S. Buecheler, and A. Tiwari, in IEEE 43rd Photovoltaic Specialists Conference (PVSC) (2016).

[16]G. Sozzi, S. Di Napoli, R. Menozzi, B. Bissig, S. Buecheler, and A. Tiwari, Sol. Energy Mater. Sol. Cells **165**, 94–102 (2017).

[17]A. Benmira and M. Aida, "Analytical modeling and simulation of CIGS solar cells," Energy Procedia **36**, 618–627 (2013).

[18]W. Metzger, R. Ahrenkiel, J. Dashdorj, and D. Friedman, Phys. Rev. B **71**, 035301 (2005).

[19]R. Klenk, Thin Solid Films **387**, 135–140 (2001).

[20]J. Pettersson, C. Platzer-Björkmann, U. Zimmermann, and M. Edoff, Thin Solid Films **519**, 7476–7480 (2011).

[21]I. Riedel, J. Keller, J. Parisi, T. Dalibor, and A. Avellan, Phys. B: Condens. Matter **439**, 9–13 (2014).

[22]J. Palm, T. Dalibor, R. Lechner, S. Pohlner, R. Verma, R. Dietmüller, A. Heiß, H. Vogt, and F. Karg, in *29th European Photovoltaic Conference Proceedings* (2014), pp. 1433–1438.

[23]T. Dalibor, S. Jost, H. Vogt, A. Heiß, S. Visbeck, T. Happ, J. Palm, A. Avellán, T. Niesen, and F. Karg, in *Proceedings of 26th EUPVSEC* (2011), pp. 2407–2411.

[24]D. K. Schroder, *Semiconductor material and device characterization* (John Wiley, New Jersey, 2006), Vol. 1.

[25]J. Schoneberg, M. Richter, J. Ohland, P. Eraerds, T. Dalibor, and J. Parisi, Thin Solid Films **633**, 243–247 (2017).

[26]Synopsys, Synopsys Sentaurus TCAD, 2017.

[27]A. Pimentel, E. Fortunato, A. Goncalves, A. Marques, H. Aguas, L. Pereira, I. Ferreira, and R. Martins, Thin Solid Films **487**, 212–215 (2005).

[28]J. Orton and M. Powell, Rep. Prog. Phys. **43**, 1263 (1980).

[29]T. Walter, R. Heberholz, C. Müller, and H. Schock, J. Appl. Phys. **80**, 4411–4420 (1996).

[30]S. Siebentritt, M. Igalson, C. Persson, and S. Lany, Prog. Photovoltaics: Res. Appl. **18**, 390–410 (2010).

[31]T. Eisenbarth, T. Unold, R. Caballero, C. A. Kaufmann, and H.-W. Schock, J. Appl. Phys. **107**, 034509 (2010).

[32]Z. Djebbour, A. Darga, A. Migan Dubois, D. Mencaraglia, N. Naghavi, J.-F. Guillemoles, and D. Lincot, Thin Solid Films **511–512**, 320–324 (2006).

[33]J. Pohl and K. Albe, Phys. Rev. B **87**, 245203 (2013).

[34]A. Niemegeers, M. Burgelman, R. Herberholz, U. Rau, D. Hariskos, and H. W. Schock, Prog. Photovoltaics. Res. Appl. **6**, 407–421 (1998).

[35]S. Siebentritt, Sol. Energy Mater. Sol. Cells **95**, 1471–1476 (2011).

[36]S. Hegedus and W. Shafarman, Prog. Photovoltaics: Res. Appl. **12**, 155–176 (2004).

[37]M. Richter, M. Hammer, T. Sonnet, and J. Parisi, Thin Solid Films **633**, 213–217 (2017).

[38]R. Scheer and H. Schock, *Chalcogenide Photovoltaics* (Wiley-VCH, 2011), pp. 29–32.

[39]M. Maiberg, T. Hölscher, S. Zahedi-Azad, W. Fränzel, and R. Scheer, Appl. Phys. Lett. **107**, 122104 (2015).

[40]D. Hauschild, Ph.D. thesis, Julius-Maximilians-Universität Würzburg, 2015.

[41]T. Magorian Friedlmeier, P. Jackson, A. Bauer, D. Harsikos, O. Kiowski, R. Menner, R. Würz, and M. Powalla, Thin Solid films **633**, 13–17 (2017).

[42]C. Durante Rincon, E. Hernandez, M. Alonso, M. Garriga, S. Wasim, C. Rincon, and M. Leon, Mater. Chem. Phys. **70**, 300–304 (2001).

[43]P. D. Paulsen, R. W. Borkmire, and W. N. Shafarman, J. Appl. Phys. **94**, 879–888 (2003).

[44]P. Jackson, R. Wuerz, D. Hariskos, E. Lotter, W. Witte, and M. Powalla, Phys. Status Solidi RRL **10**, 583–586 (2016).